Mechanical performance of additively manufactured lightweight cellular solids: Influence of cell pattern and relative density on the printing time and compression behavior

Albert Forés-Garriga, Giovanni Gómez-Gras, Marco A. Pérez *

IQS School of Engineering, Universitat Ramon Llull, Via Augusta 390, 08017 Barcelona, Spain

HIGHLIGHTS

- A broad spectrum of specific stiffness and strength is achieved from the infill pattern and density.
- Validated equations are given to estimate the relative density, stiffnesses and strengths.
- Manufacturing defects reveal the need to implement strategies to optimize printing trajectories.
- Sparse infill provides comparable performance with a considerably shorter manufacturing time.

GRAPHICAL ABSTRACT
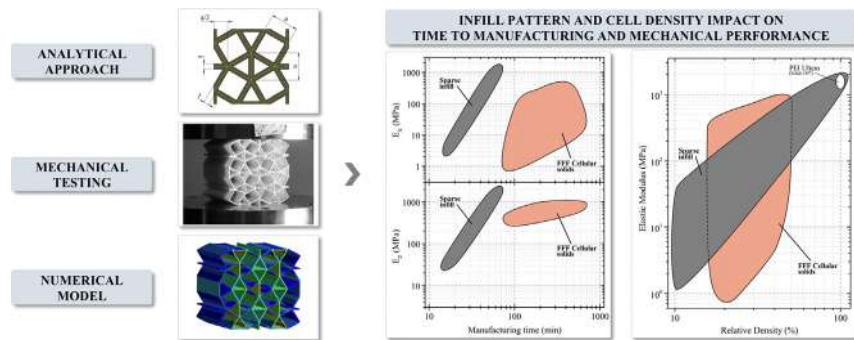
ABSTRACT

A comprehensive investigation is presented on the Fused Filament Fabrication (FFF) technology's possibilities to create cellular solids with a broad spectrum of specific stiffness and strength, modifying cell geometry and size, while addressing manufacturing matters such as inherent defects and built time. Thirteen typologies of two-dimensional cellular patterns with different relative densities are examined. Results have allowed conclusions to be drawn regarding the influence of cell type and infill density on mechanical performance. Intra-layer and inter-layer inherent defects identified after manufacturing highlight the importance of optimizing filament trajectories. A reliable comparison of the elastic properties of the cellular patterns as a function of their density is presented. An experimentally validated numerical model is provided for predicting the compression stiffness of the different cell patterns with an average deviation below 5%. The model can reproduce the behavior in the elastic range based on tensile specimen properties and a Normal Stiffness Factor to account for the phenomenon of elastic asymmetry of the FFF printed samples. The wide range of results achieved is experimental confirmation of the potential of FFF cellular solids. Lastly, this investigation provides analytical, numerical, and empirical validated evidence to further design-for-additive manufacturing strategies with cellular solids for designing advanced lightweight structures.

© 2022 The Authors. Published by Elsevier Ltd. This is an open access article under the CC BY-NC-ND license (http://creativecommons.org/licenses/by-nc-nd/4.0/).

1. Introduction

Cellular solids are defined as those made up of an interconnected network of solid struts or plates that form the edges and faces of cells, packed together to fill space [1]. Basically, there are

* Corresponding author.
E-mail address: marcoantonio.perez@iqs.url.edu (M.A. Pérez).

two broad classes of cellular solids: one consists of a stochastic structure such as foams, whereas the other is composed of a periodic structure such as lattice truss and prismatic structures. Its properties depend directly on cells' shape and connectivity and the specific solid material they are made. The single most important feature of a cellular solid is its relative density, which is the quotient between the density of the cellular solid and the one of the solid material of which it is made.

Cellular solids appear in many natural materials and structures, such as cancellous bone, wood, cork, or sponges [2–4]. Man has used natural cellular materials for centuries since they have physical, mechanical, and thermal outstanding properties compared to fully dense solids. The human-made cellular solids exploit the unique combination of properties for a wide range of engineering applications, such as the low density, which allows the design of light and stiff components such as sandwich panels; the low thermal conductivity for manufacturing effective thermal insulation; or the low strength and large compressive strains which make them attractive for energy-absorbing applications [5–10].

Recent advances in additive manufacturing (AM) technologies have widened the horizons of the fabrication possibilities and application of cellular solids [11–18]. A major advantage of the AM technologies is its feasibility to fabricate lighter structures with a wide range of materials, printing the parts with solid shells filled with low-density infill. Accordingly, the infill stands as a manufacturing parameter that plays a significant role in the strategy to reduce weight, time to print, and print cost but also to design structures with tailored properties [19,20]. This provides AM an outstanding competitive advantage as compared to other conventional manufacturing technologies.

An additively manufactured part's infill density is an important design factor directly related to the cell size. The parameter can be adjusted as a percentage of filling or by controlling the internal raster-to-raster air gap. It has been shown that infill density has a noticeable effect on weight reduction, manufacturing time, and cost, but also on stiffness and strength of the printed part. Nevertheless, infill geometry defined by cell shape can play even a more significant role in the printed part's mechanical performance since it could allow producing components with tailored functional characteristics [21–27]. For example, when the cells are equiaxed, the properties are isotropic, but when the cells are even slightly elongated or flattened, the properties depend on the direction, presenting an orthotropic or even an auxetic behavior. Hence, if such parts are to be used in load-bearing components, understanding their mechanics is of utmost importance for an optimal design.

Several studies on the mechanical behavior of cellular solids manufactured by AM and, in particular, by Fused Filament Fabrication (FFF) can be found in the literature. Overall, the different works mainly investigate their mechanical behavior through numerical approaches, with some experimental validation examples [28–33]. These studies analyze the effect of infill density on mechanical performance by modifying the cell size, or the effect of infill geometry by changing the cell typology. In general, the studies focus on compression behavior and mostly on analyzing the auxetic behavior induced by cell geometry [34–51]. Other researchers have investigated the combination of different infill cells, creating the so-called hierarchical cell geometries with promising results [52–55]. However, most studies are bounded to analyzing some particular cell geometry or numerical modeling of various cell typologies, establishing comparisons based on their performance. Hence, in the authors' opinion, there is a need for more comprehensive research. Firstly, to explore FFF technology's possibilities to create multiple cellular solids able to broaden the spectrum of specific stiffness and strength from one single material. Secondly, to study the primary cell geometries together with the effect of cell size from a mechanical performance point of view,

but also considering manufacturing issues, thus aimed to contribute to strengthen AM cellular solids designs' feasibility.

Accordingly, the purpose of this work is to investigate the role of the infill density together with the pattern geometry on the mechanical performance and weight reduction of cellular solids manufactured by FFF. The work is focused on two-dimensional geometries, thus avoiding the use of support material. This study aims to provide analytical, numerical, and experimental validated evidence to further contribute to design-for-additive manufacturing strategies with cellular solids, with an in-deep analysis of the infill's mechanical performance and addressing manufacturing matters, such as inherent defects and built time.

2. Cell designs

Since the cell pattern plays an essential role in the cellular solid's physical and mechanical properties [1], a broad and a representative number of the principal two-dimensional cell shapes found in the literature are examined in this work. In particular, the analysis encompasses the two-dimensional cell shapes Antitetrachiral, Circular, Hexachiral, Hexagon, Re-Entrant Hexagon type I and II, Lozenge Grids, Rotachiral, Sinusoidal Ligaments, Square Grids, SrCuBO, and Tetrachiral. The infill so-called Sparse, widely used in FFF printing strategies, has also been included for comparison. Fig. 1 depicts the unit cell shapes and a representative manufactured sample of each infill pattern assessed. Sub-figure s corresponds to a solid cube sample made by the same material as the cell walls, the results of which will be used for comparison.

As stated before, the single most important feature of a cellular solid is its relative density, which is the quotient between the density of the cellular solid (ρ^*) and the one of the solid material (ρ^s) of which it is made. Furthermore, the relative density is equivalent to the ratio between the elastic modulus along z-direction of the cellular solid and the one of the corresponding solid material [1], i.e.:

$$\frac{E_z^*}{E_z^s} = \frac{\rho^*}{\rho^s} \tag{1}$$

Generally speaking, natural cellular solids have relative densities which are less than about 30%.

The effective in-plane Young modulus (E_x^* and E_y^*) and strength (σ_x^* and σ_y^*) of two-dimensional lattice structures can be also estimated from the relative density and the Young modulus of the solid E^s. In particular, the scaling laws can be adequately represented by the power-law expressions [56]:

$$\frac{E_x^*}{E_x^s} = B_x \left(\frac{\rho^*}{\rho^s}\right)^b \qquad \frac{E_y^*}{E_y^s} = B_y \left(\frac{\rho^*}{\rho^s}\right)^b \tag{2}$$

$$\frac{\sigma_x^*}{E_x^s} = C_x \left(\frac{\rho^*}{\rho^s}\right)^c \qquad \frac{\sigma_y^*}{E_y^s} = C_y \left(\frac{\rho^*}{\rho^s}\right)^c \tag{3}$$

where $b = 1$ and $c = 1$ for stretch-dominated structures; $b = 3$ and $c = 2$ for bending-dominated structures; and B_x, B_y, C_x, and C_y are experimental coefficients that depend on the pattern cell geometry. This classification does not consider the overall effect of shear, hinging, and flexural stiffness; however, the predictions are reasonably acceptable. Although there are some works in the literature that provide some of these experimental factors, very few cell patterns are reported [1,23,56,57].

Given the relevance of relative density, in this work each cell shape's geometrical design has been parameterized with the variables indicated in Fig. 1. In this way, modifying the design parameters allows the building of cellular solids with different infill densities while keeping the cell pattern. Considering these design
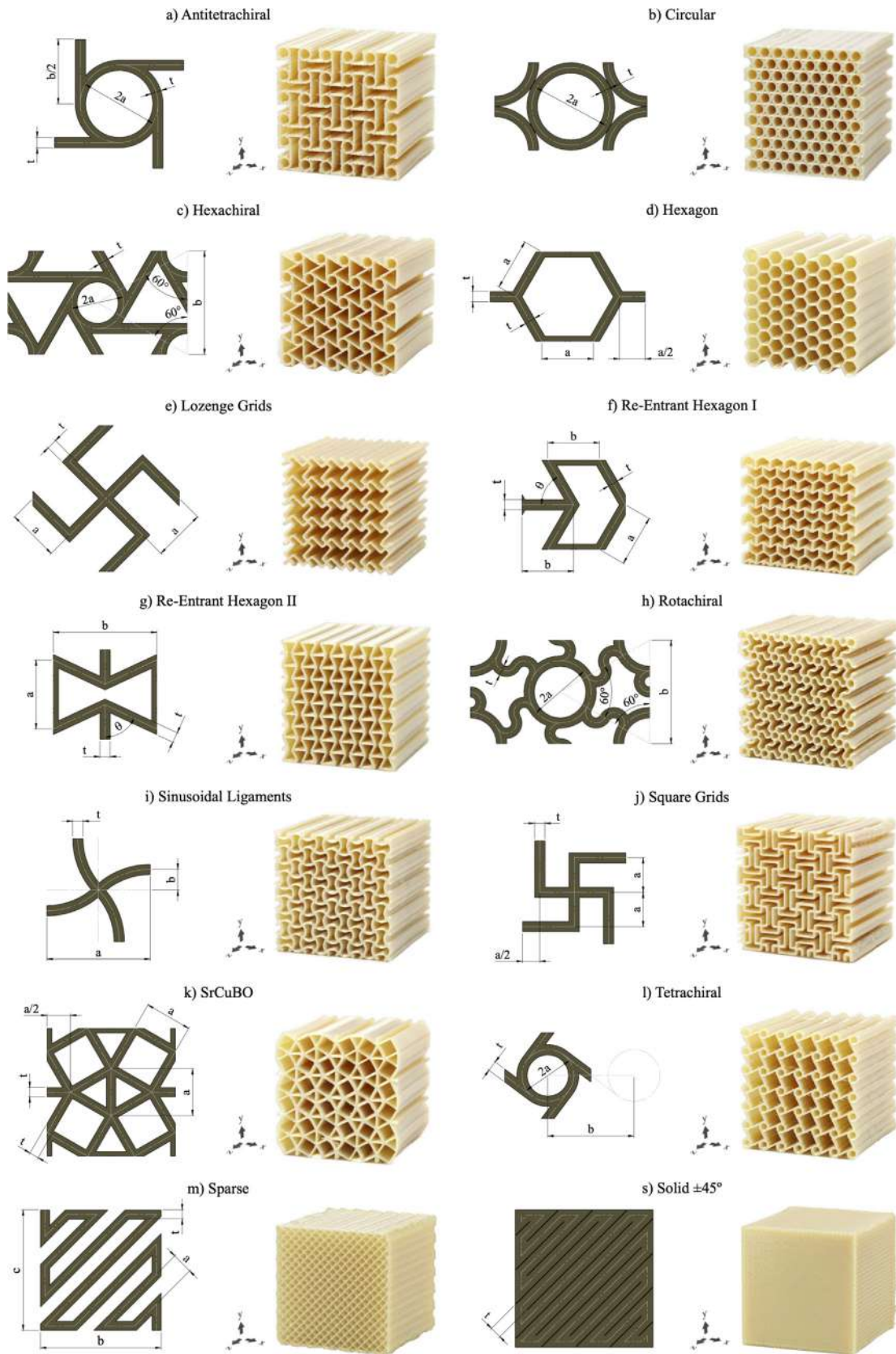
Fig. 1. Unit cell shapes design and corresponding FFF manufactured sample of each infill pattern assessed.

parameters, the analytical equations for the relative density of all the infill patterns have been determined, as shown below:

(a) Antitetrachiral

$$\frac{\rho^*}{\rho^s} = \frac{2}{b^2}\left[t(a\pi + b) + \frac{\sqrt{2}}{2}(2a-t)\sqrt{at} - \left(a+\frac{t}{2}\right)^2 \arccos\left(\frac{2a-t}{2a+t}\right)\right] \tag{4}$$

(b) Circular

$$\frac{\rho^*}{\rho^s} = \frac{4}{\sqrt{3}}\frac{at\pi}{(2a+t)^2} \tag{5}$$

(c) Hexachiral

$$\frac{\rho^*}{\rho^s} = 1 - \frac{1}{b^2}\left[\frac{2\pi}{\sqrt{3}}\left(a-\frac{t}{2}\right)^2 + \left(\sqrt{b^2-4a^2} - t\sqrt{3}\right)^2\right] \tag{6}$$

(d) Hexagon

$$\frac{\rho^*}{\rho^s} = \frac{t\sqrt{3}}{9a^2}\left(6a - t\sqrt{3}\right) \tag{7}$$

(e) Lozenge Grids

$$\frac{\rho^*}{\rho^s} = \frac{8a-t}{8a^2}t \tag{8}$$

(f) Re-Entrant Hexagon I

$$\frac{\rho^*}{\rho^s} = 1 - \frac{\left(a\sin\theta - \frac{t}{2}\right)\left(b - \frac{t}{\sin\theta}\right)}{ab\sin\theta} \tag{9}$$

(g) Re-Entrant Hexagon II

$$\frac{\rho^*}{\rho^s} = \frac{2t\left[a + \frac{1}{\sin\theta}(b-t) - \frac{t^2}{2\tan\theta}\right]}{b\left(2a - \frac{b}{\tan\theta}\right)} \tag{10}$$

(h) Rotachiral

$$\frac{\rho^*}{\rho^s} = \frac{\pi t(3b-2a)}{\sqrt{3}b^2} + \frac{\sqrt{3at(b-2a)(2a+b+2t)}}{\sqrt{2}b^2} - \\ -\frac{2\sqrt{3}}{b^2}\left(\frac{b}{4} - \frac{a}{2} + \frac{t}{2}\right)^2 \arccos\left(\frac{b^2+2bt-4a^2-12at}{[b+2(t-a)](2a+b)}\right) - \\ -\frac{2\sqrt{3}}{b^2}\left(a + \frac{t}{2}\right)^2 \arccos\left(\frac{6at+2ab+4a^2-bt}{(2a+t)(2a+b)}\right) \tag{11}$$

(i) Sinusoidal Ligaments

$$\frac{\rho^*}{\rho^s} = \frac{4}{a^2}\left[\left(b-\frac{t}{2}\right)^2 + \left(b-\frac{t}{2}+\Psi\right)\left(\frac{a}{2} - b + \frac{t}{2}\right) + \left(\frac{a}{2}-\Psi\right)\left(\Omega - b + \frac{t}{2}\right)\right] + \\ +\frac{2}{a^2}\left[\left(\frac{a^2}{8b} + \frac{b}{2} + \frac{t}{2}\right)^2(2\gamma - \sin(2\gamma)) - \left(\frac{a^2}{8b} + \frac{b}{2} - \frac{t}{2}\right)^2(2\delta - \sin(2\delta))\right] \tag{12}$$

where:

$$\alpha = \arcsin\left(\frac{\sqrt{2}\left(a^2 - 4b^2 - 4ab\right)}{2\left(4b^2 + a^2\right)}\right)$$

$$\beta = \arccos\left(-\frac{\sqrt{2}\left(-16b^4 - 32tb^3 - 8a^2b^2 - 8bta^2 - a^4\right)}{2\left(4b(b+t)+a^2\right)\left(4b^2+a^2\right)}\right)$$

$$\gamma = \arcsin\left(\frac{\frac{a}{2} - \Psi}{\frac{a^2}{8b} + \frac{b}{2} + \frac{t}{2}}\right)$$

$$\delta = \arcsin\left(\frac{\frac{a}{2} - \Omega}{\frac{a^2}{8b} + \frac{b}{2} - \frac{t}{2}}\right)$$

$$\Psi = \frac{a}{2} - \left(\frac{a^2}{8b} + \frac{b+t}{2}\right)\cos\left(\frac{\pi}{2} + \alpha - \beta\right)$$

$$\Omega = -\frac{a^2}{8b} + \frac{b}{2} + \left(\frac{a^2}{8b} + \frac{b+t}{2}\right)\sin\left(\frac{\pi}{2} + \alpha - \beta\right)$$

(j) Square Grids

$$\frac{\rho^*}{\rho^s} = \frac{10a-t}{9a^2}t \tag{13}$$

(k) SrCuBO

$$\frac{\rho^*}{\rho^s} = \frac{20at - t^2\left(4 + 6\sqrt{3}\right)}{a^2\left(4 + 2\sqrt{3}\right)} \tag{14}$$

(l) Tetrachiral

$$\frac{\rho^*}{\rho^s} = \frac{2}{b^2}\left[t\left(a\pi + 2\sqrt{\left(\frac{b}{2}\right)^2 - a^2}\right) - \left(a+\frac{t}{2}\right)^2 \arccos\left(\frac{2a-t}{2a+t}\right)\right] + \\ +\frac{\sqrt{2}}{b^2}(2a-t)\sqrt{at} \tag{15}$$

(m) Sparse

$$\frac{\rho^*}{\rho^s} = \frac{bc + a(b+c-t)}{bc(t+a)}t$$

3. Methodology

3.1. Manufacturing of samples

To investigate the infill density's role together with the infill geometry on the mechanical performance and weight reduction of cellular solids, the thirteen above designs were evaluated with three different density levels, except for the Sparse type, for which six air gap values were considered, thus providing a total of 42 different filling configurations. Table 1 collects the design parameters selected for each configuration. Cell wall-thickness t was set to 0.508 mm for all configurations. An integer number of complete unit cells was settled to get a cubic specimen whose dimensions were as close as possible to $40 \times 40 \times 40$ mm.

Specimens were manufactured in a Stratasys Fortus 400mc FDM equipment using PEI Ultem 9085 material. This printer has a chamber that controls the temperature during the whole manufacturing process, improving the inter-layer adherence between adjacent building layers [19]. The optimum operating conditions for processing PEI Ultem require an oven temperature of 195 °C, while the extrusion temperature for the model material was set to 380°C. Insight 3D Printing Software (Stratasys) was used for the G-code generation. Samples were manufactured with a slice height of 0.254 mm and a nominal wall-thickness t of just one contour of 0.508 mm. This fact reduces the required material for building each cell pattern and its manufacturing time. Sparse patterns were created by including a separation between intra-layer filaments with the raster-to-raster air gap parameter. Due to the two-dimensional design of the unit cells and the upright orientation, no support material was necessary as geometries can stand by itself while building, which directly benefits the manufacturing time and material consumption. The estimated manufacturing time for each configuration is provided in Table 1.

Two samples were printed for each configuration and testing orientation, leading to a total of 198 samples. Once printed, samples were examined using a high-resolution Olympus DSX1000 digital microscope to assess the manufacturing process and identify possible defects. In addition, the mass and the nominal external dimensions of each manufactured sample were measured, and their density was determined. The experimental relative density was then calculated by dividing the average result of every considered infill pattern over the solid configuration value. These results are summarized in Table 1, where minor differences are noticed between the experimental relative density results and the corresponding analytical ones calculated with the equations Eq. (4)–(16).

Table 1
Design parameters, manufacturing time, and analytical and experimental relative densities.

Pattern	Density Level	Design dimensions			Manufacturing time (min)	Relative density (%)	
		a (mm)	b (mm)	θ (°)		Anal.	Exp.
(a) Antitetrachiral	I	1.30	4.00	-	608	46.07	44.58
	II	2.00	7.00	–	258	26.41	25.32
	III	2.75	10.00	–	111	18.73	16.60
(b) Circular	I	1.70	–	–	381	45.04	47.64
	II	2.20	–	–	206	37.22	40.18
	III	3.20	–	–	212	27.55	34.21
(c) Hexachiral	I	1.30	5.20	–	522	40.91	38.61
	II	1.90	7.50	–	265	30.16	27.18
	III	2.50	10.00	–	172	23.59	21.81
(d) Hexagon	I	2.35	–	–	265	26.37	25.25
	II	2.85	–	–	157	22.04	21.50
	III	3.85	–	–	98	16.58	16.44
(e) Lozenge Grids	I	1.70	–	–	205	32.54	32.60
	II	2.20	–	–	127	25.40	24.76
	III	2.70	–	–	101	20.83	20.90
(f) Re-Entrant Hexagon I	I	2.35	2.69	60	291	35.47	35.59
	II	2.85	3.19	60	217	30.17	30.02
	III	4.35	4.69	60	95	20.80	20.81
(g) Re-Entrant Hexagon II	I	3.80	5.80	65	198	38.36	37.17
	II	4.80	7.30	65	152	30.87	29.76
	III	5.80	8.30	65	100	25.55	25.33
(h) Rotachiral	I	1.25	6.00	–	488	38.86	37.22
	II	1.55	7.50	–	341	31.74	29.26
	III	2.05	10.00	–	203	24.33	23.06
(i) Sinusoidal Ligaments	I	3.00	1.00	–	434	45.35	46.15
	II	4.00	1.00	–	271	31.39	33.92
	III	6.00	1.00	–	140	19.73	20.05
(j) Square Grids	I	1.80	–	–	238	34.52	36.73
	II	2.30	–	–	157	27.21	28.72
	III	3.10	–	–	85	20.32	20.42
(k) SrCuBO	I	3.50	–	–	498	38.98	39.83
	II	5.00	–	–	249	28.39	31.38
	III	7.00	–	–	113	20.80	23.68
(l) Tetrachiral	I	1.30	5.00	–	341	30.74	28.23
	II	1.50	6.00	–	285	25.96	23.34
	III	2.00	8.00	–	148	20.09	17.15
(m) Sparse	I	0.25	–	–	45	70.66	69.13
	II	0.50	–	–	37	54.94	53.02
	III	0.75	–	–	36	45.13	42.76
	IV	1.50	–	–	27	29.88	27.71
	V	3.00	–	–	20	18.55	16.93
	VI	6.00	–	–	16	11.40	10.46
(s) Solid ±45°	S	–	–	–	66	100.00	100.00[a]

Stratasys PEI Ultem filament's density: 1.27 g/cm^3 [58].
Experimental measured wall-thickness $t = 0.5777$ mm. See Section 4.1 for more details.
[a] Experimental measured density of Solid ±45° pattern: 1.1457 g/cm^3.

3.2. Compression testing

The specimens were tested in compression in the in-plane x and y-directions, and the out-of-plane z-direction. For those symmetrical cells, such as Antitetrachiral, Lozenge Grids, Rotachiral, Sinusoidal Ligaments, Square Grids, SrCuBO, Tetrachiral, and Sparse patterns, only tests in x and z-directions were performed considering the equivalence of x and y-directions. Tests were conducted using ZwickRoell Z030 equipment (30 kN). A 3D Digital Image Correlation (DIC) was used to analyze full-field deformation. To create the speckled pattern, samples were painted with an airbrush spray gun with different tips. Microscopic analysis showed a highly contrasted, stochastic, and isotropic pattern, with an average black mark ratio of 41.7% (see Fig. 3 r). Two Allied Vision GigE MAKO G-507B cameras with APO-Xenoplan 1.4/23-0903 lenses were employed to record the samples' surface displacements. The setup's calibration was performed with a GOM CP20/MV55x44 panel, reporting a deviation of 0.024 pixels. The sequences were finally post-processed with GOM Correlate Professional software using a facet size of 19x19 pixels.

For the compression test, the ASTM C365 standard [59] was followed with a crosshead rate of 3 mm/min, so that specimen failure occurred during 3 and 6 min of testing, according to the standard specification. The results of elastic modulus, first peak stress, and energy absorption up to first peak load were reported for each test direction. For stress calculations, the specimen's nominal external dimensions were considered. The Poisson's ratios were determined as the ratio between the two in-plane displacement components using DIC extensometers placed at a quarter (10 mm) and three-quarters (30 mm) of the specimen's height.

3.3. Finite element model

An Ansys FE implicit model was created to evaluate the elastic performance of each cellular geometry numerically. The pattern was directly imported in STEP format. Two rigid bodies were created on the top and bottom faces to represent compression test plates. Cellular geometries were meshed with 30 divisions in the z-direction (building direction) and with an element's size of 0.15 mm in the manufacturing plane. Higher-order 3D 20-node solid element SOLID186 was used. As a model example, Fig. 2 depicts the mesh for the Antitetrachiral pattern with density level II.

Displacements and rotations were restricted to fix the bottom plate, while a 0.1 mm displacement was imposed on the upper plate along the loading testing direction. Frictional contacts with asymmetric behavior were defined between the cellular pattern and the plates. According to PEI Ultem 1010 available datasheets [60], the friction coefficient was set to 0.42. The Augmented Lagrange formulation with a penetration tolerance of 0.1 mm was activated, and ramped effects were permitted. The reaction force was finally measured on the bottom surface to evaluate the stiffness of the cellular pattern.

The properties of the cell walls' material were adopted from a previous comprehensive study [19] on the material PEI Ultem
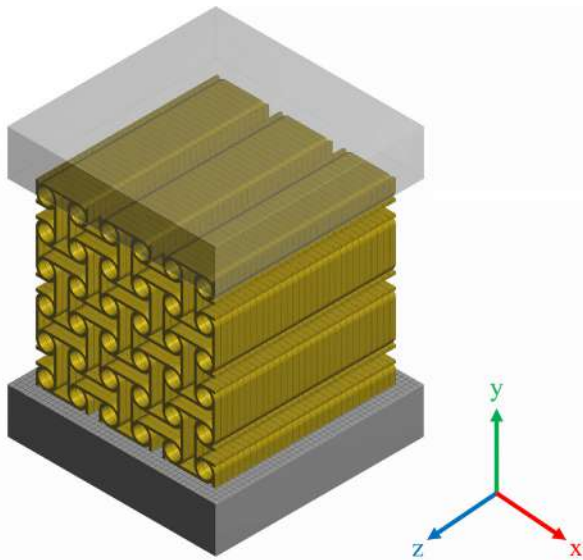

Fig. 2. Boundary conditions and generated mesh example of the FE model developed for the numerical simulation of the compression behavior of the cellular solid patterns.

9085, where tensile, flexural, and shear behaviors were determined for different Solid and Sparse infill configurations. Main results of the Solid $\pm 45°$ infill configuration are depicted in Table 2. In this case, three scenarios were examined on the simulations: orthotropic, quasi-isotropic and isotropic material. Since several authors have demonstrated the elastic asymmetry of FFF printed parts [61,62] due to the contribution of the filament bonds, the given properties needed to be adapted to the compression behavior. Hence, to reproduce the phenomenon of elastic asymmetry, the Normal Stiffness Factor (FKN) was included in the contacts' definition. FKN factors were calibrated from the Solid $\pm 45°$ cube (Fig. 1 s) experimental results for the in-plane and the out-of-plane test, obtaining values of 0.215 and 0.050, respectively. With these FKN factor settings and defining the material with tensile and shear properties, the FE model described the FFF asymmetric compression elastic behavior with an accuracy of 99% when compared to the experimental results. The adjusted model was then used to simulate all the cellular patterns studied in each of the test directions.

The Sparse pattern was automatically created from a solid CAD part in Insight software,. In other words, the detailed pattern geometry was not available as in the other cells thus requiring a different model approach. Accordingly, the Representative Volume Element (RVE) method was adopted with homogeneous material properties recalculated using the obtained analytical model, as follows:

$$E_x^{sp} = \eta_2 E_x^s \quad E_y^{sp} = \eta_2 E_y^s \quad E_z^{sp} = \eta_3 E_z^s \tag{17}$$

$$v_{xy}^{sp} = \eta_1 v_{xy}^s \quad v_{yz}^{sp} = \eta_1 v_{yz}^s \quad v_{xz}^{sp} = \eta_1 v_{xz}^s \tag{18}$$

$$G_{xy}^{sp} = \eta_2 G_{xy}^s \quad G_{yz}^{sp} = \eta_3 G_{yz}^s \quad G_{xz}^{sp} = \eta_3 G_{xz}^s \tag{19}$$

$$\sigma_{T,x}^{sp} = \eta_1 \sigma_{T,x}^s \quad \sigma_{T,y}^{sp} = \eta_1 \sigma_{T,y}^s \quad \sigma_{T,z}^{sp} = \eta_1 \sigma_{T,z}^s \tag{20}$$

$$\sigma_{C,x}^{sp} = \eta_1 \sigma_{C,x}^s \quad \sigma_{C,y}^{sp} = \eta_1 \sigma_{C,y}^s \quad \sigma_{C,z}^{sp} = \eta_1 \sigma_{C,z}^s \tag{21}$$

$$\tau_{xy}^{sp} = \eta_1 \tau_{xy}^s \quad \tau_{yz}^{sp} = \eta_1 \tau_{yz}^s \quad \tau_{xz}^{sp} = \eta_1 \tau_{xz}^s \tag{22}$$
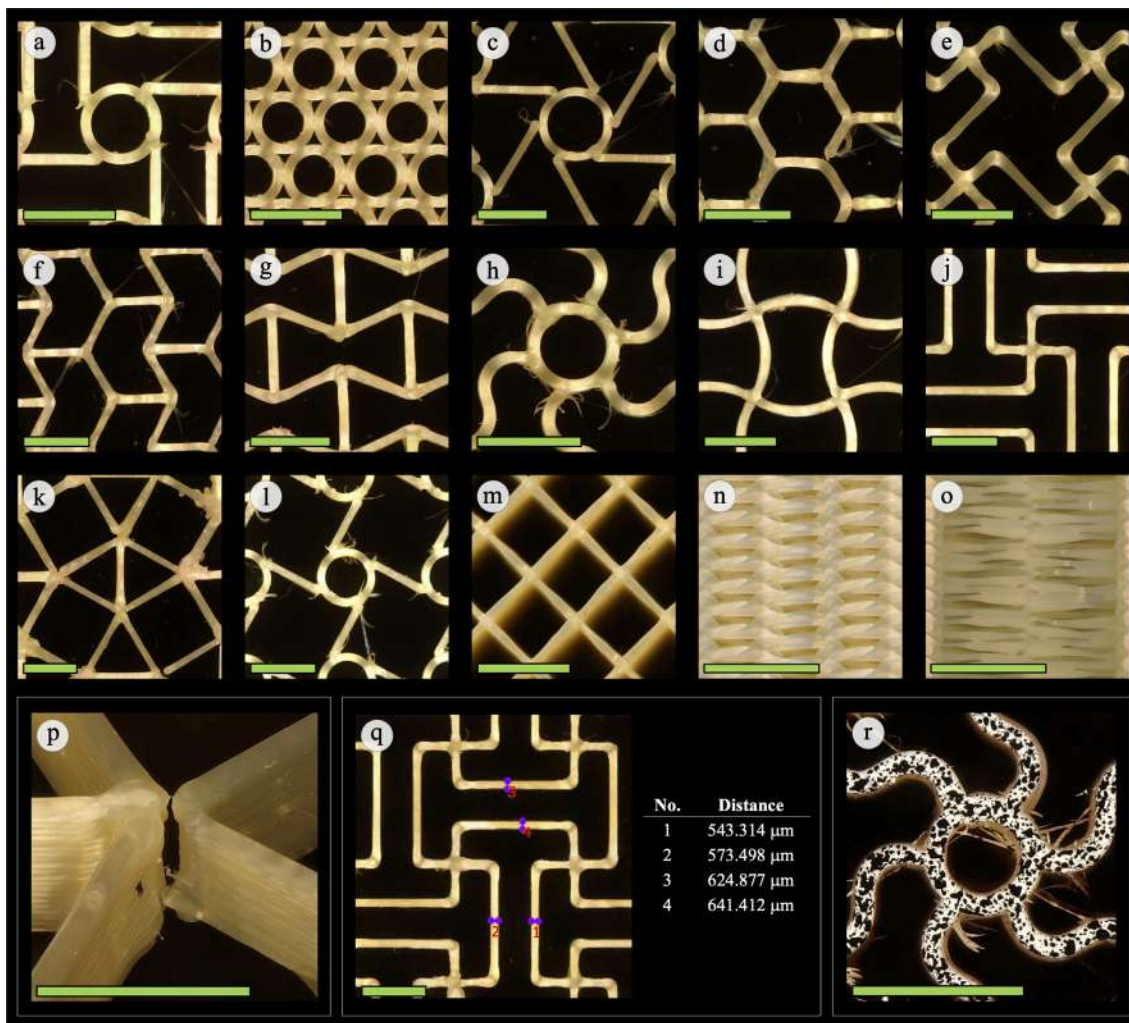
where the minoring factor $\eta_1 = \frac{\rho^*}{\rho^s}$ is taken from Eq. 16, $\eta_2 = \frac{E_x^*}{E_x^s} = \frac{E_y^*}{E_y^s}$ from Eq. 23, and $\eta_3 = \frac{E_z^*}{E_z^s}$ from Eq. 24. Superscript ^{sp} states Sparse properties, and superscript ^{s} refers to the properties of the solid material in $\pm 45°$ printing configuration evaluated with tensile and shear tests (extracted from [19]).

4. Results and discussion

4.1. Microscopy analysis

4.1.1. Cell wall-thickness

The panel in Fig. 3 shows microscopic details of the intra-layer joints of each manufactured cellular pattern, inter-layer defects, and measurements of the thickness of the deposited filament.

Table 2
PEI Ultem elastic properties and stress limits used on the FE model.

Orthotropic Elasticity					Orthotropic Stress Limits				
Property	Symbol	Iso.	Q-Iso.	Ortho.	Property	Symbol	Iso.	Q-Iso.	Ortho.
Young's Modulus x-direction (MPa)	E_x^s	2123	2121	2092	Tensile x-direction (MPa)	$\sigma_{T,x}^s$	24.46	24.45	26.50
Young's Modulus y-direction (MPa)	E_y^s	2123	2121	2150	Tensile y-direction (MPa)	$\sigma_{T,y}^s$	24.46	24.45	22.40
Young's Modulus z-direction (MPa)	E_z^s	2123	2126	2126	Tensile z-direction (MPa)	$\sigma_{T,z}^s$	24.46	24.48	24.48
Poisson's Ratio xy	v_{xy}^s	0.368	0.344	0.344	Compressive x-direction (MPa)	$\sigma_{C,x}^s$	−24.46	−24.45	−26.50
Poisson's Ratio yz	v_{yz}^s	0.368	0.392	0.392	Compressive y-direction (MPa)	$\sigma_{C,y}^s$	−24.46	−24.45	−22.40
Poisson's Ratio xz	v_{xz}^s	0.368	0.392	0.392	Compressive z-direction (MPa)	$\sigma_{C,z}^s$	−24.46	−24.48	−24.48
Shear Modulus xy (MPa)	G_{xy}^s	704	630	630	Shear xy (MPa)	τ_{xy}^s	25.86	25.72	25.72
Shear Modulus yz (MPa)	G_{yz}^s	704	741	745	Shear yz (MPa)	τ_{yz}^s	25.86	25.93	27.37
Shear Modulus xz (MPa)	G_{xz}^s	704	741	737	Shear xz (MPa)	τ_{xz}^s	25.86	25.93	24.48

Fig. 3. Microscopic detail of the intra-layer joints - Antitetrachiral (*a*), Circular (*b*), Hexachiral (*c*), Hexagon (*d*), Lozenge Grids (*e*), Re-Entrant Hexagon I (*f*), Re-Entrant Hexagon II (*g*), Rotachiral (*h*), Sinusoidal Ligaments (*i*), Square Grids (*j*), SrCuBO (*k*), Tetrachiral (*l*), Sparse in-plane (*m*) and out-of-plane (*n-o*), inter-layer defects (*p*), measurements of the thickness of the filament (*q*), and DIC speckle pattern (*r*). Scale bar is 5 mm.

In Section 3.1, it is defined that the nominal cell wall-thickness *t* was set to 0.508 mm for all configurations. This value is commanded by the FFF tip used (here T16 with a nozzle diameter of 0.016 in or 0.4064 mm), whose size conditions the slice height (0.010 in or 0.254 mm) and the width of the extruded filament (approximately twice the height, i.e., 0.020 in or 0.508 mm). Nevertheless, as specified in Table 1, the value used for calculating the relative density from the analytical Eq. 4–16 was *t* = 0.5777 mm (±0.0110 mm). This value corresponds to the average result measured on the microscopic analysis of the cell walls of printed samples (see image *q* in Fig. 3).

4.1.2. Manufacturing defects

Apart from the irregular filaments' thickness, the images in Fig. 3 also show some discontinuities in the trajectories in both the in-plane (intra-layer) and the out-of-plane (inter-layer) filament joints. Intra-layer joints are detailed in sub-figures *a-m*. As can be noted, deposited rasters' quality depends on the trajectories required to create the patterns. In those cases where circumferences appear in the pattern's cellular unit, the extruder head first creates the circles and later connects them with the bars (see Fig. 3 *a*, c, h, and *l*). As a result, the raster's joint that closes each circumference is almost unnoticeable, while the finish of the connec-

tions between these circles and the toolpaths that link the different cells is notably lower.

Defects in connections are more evident in some patterns formed by rectilinear trajectories. In such cases, the requirements to repeatedly pass over the same point to build the whole pattern led to several material blobs (see Fig. 3 *k*). Besides, the abrupt changes of direction of the nozzle or the end of the trajectory create deficiencies in cell-cell bonding (see Fig. 3 *d*), which could affect the mechanical performance. In contrast, the pattern's quality is highly improved in those cases that take advantage of the optimized toolpaths by reducing the amount of intra-layer unions such as the Sparse (see Fig. 3 *m*).

When successive in-plane imperfections occur in the same location for adjacent layers, an inter-layer defect appears, as shown in Fig. 3 *p*. This discontinuity has proved to dramatically impact the pattern's mechanical behavior when tested in the in-plane directions.

To prevent these inter-layer defects, it would be necessary to have a different start of each layer's path to avoid overlapping seams and force each layer's paths to be different. The last was not an option available in the Insight 3D Printing Software, so defects were not avoidable for these particular cell geometries. A compromise solution would be to increase the wall-thickness or

geometrically reinforce the joint, both of which would result in an undesirable increase in relative density of the cellular solid.

4.1.3. Sparse infill

The case of the Sparse infill deserves special consideration. Unlike the rest of the geometries in which the extruded filament is deposited over the preceding layer's filament, there is a 90° rotation of the toolpaths between two adjacent layers in the Sparse pattern when a raster angle of ±45° is employed. This fact causes inter-layer voids, as shown in Fig. 3 (n-o), whose magnitude increases as the air gap grows. This phenomenon causes a weakening of the stiffness in the out-of-plane direction (z-direction), as proved later, but essentially reduces the manufacturing time and material consumption, as shown in the next section, thus becoming an efficient solution for low-density infill.

4.2. Experimental analysis

4.2.1. Compressive behavior

Fig. 4 shows a representative example of load-displacement curves for the three levels of density of the Hexachiral and Re-Entrant Hexagon I patterns. The results presented were obtained from compression testing along x-direction (see Fig. 1). The results state a clear impact of both the pattern and the cell's dimensions on the mechanical behavior, as expected. In particular, the stiffness and the first detected peak load results vary significantly between the examined configurations.

Results obtained from the experimental compressive evaluation of the manufactured cellular patterns are summarized in Table 3. Elastic modulus values are given for the three orthogonal directions, and Poisson's Ratios (v_{xy} and v_{yx}), first peak stress and energy absorption efficiency data acquired in the in-plane tests are provided. Poisson's ratios are reported in the same strain range used to calculate the elastic moduli ($\varepsilon = 0.1\% - 0.3\%$). Nominal external
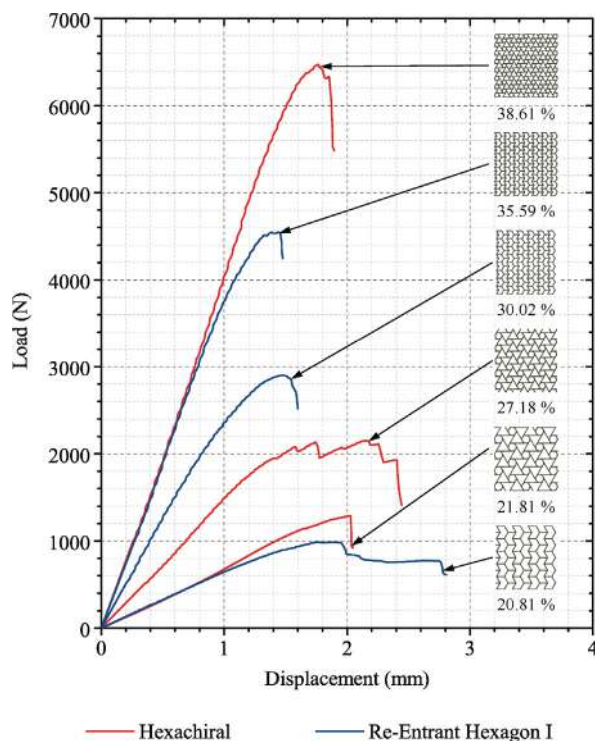
dimensions were used for the calculation of the engineering properties, and energy absorption efficiency was calculated by relating the total amount of energy absorbed up to the first peak of load with the material volume estimated in the Insight 3D Printing Software. Finally, the adjusted coefficients B and C for the power-law expressions (see Eq. 2–3) are included together with the corresponding Coefficient of determination (R^2) in Table 3.

On the one hand, compression testing results show a clear difference between the in-plane and the out-of-plane behavior. In particular, the z-direction's elastic moduli results exceed those in the x and y orientations by one order of magnitude in most cases. Moreover, the DIC post-process allowed detecting that the in-plane tests' failure of the patterns was initiated at the intra-layer joints that arise from the FFF manufacturing toolpaths. Hence, as proved in a previous work [19], the intra-layer unions are weakened points that can limit the maximum reachable load.

On the other hand, the different density levels' trends confirm the effect of mass decrease on the mechanical properties of the cellular solids. As can be gathered from the values in Table 3, both the elastic modulus and the maximum load decrease with the density of the pattern, as expected. However, the energy absorption efficiency does not always follow the same trend. A clear example of this is shown by the Sparse infill, where density level IV (air gap 1.50 mm) has delivered 2.28 times the energy efficiency of level I (air gap 0.25 mm).

4.2.2. Mechanical performance versus manufacturing time

Results trends differ even more if the mechanical properties are related to each sample's printing time. It is considered a relevant issue when contemplating manufacturing lightweight components with cellular solid designs while preserving their feasibility from the fabrication perspective. Fig. 5 and Fig. 6 depict the obtained elastic modulus and energy absorption efficiency results versus the manufacturing time of each pattern, respectively.

Data presented in Fig. 5 and Fig. 6 confirm a manufacturing advantage of the Sparse over the rest of the infill patterns. As shown, the optimization of the printing toolpaths of the Sparse pattern reduces the time needed for their construction by at least one order of magnitude. In addition, the results of elastic moduli show a clear trend towards the solid cube result as the air gap parameter decreases (see Table 1). It should be seen that the main differences in the elastic modulus correspond to the E_z. This is due to the filaments' arrangement between two adjacent layers, which produces an inter-layer weakness, as observed in Fig. 3 (n-o).

It should be noted that the Sparse design simplifies the manufacturing trajectories compared to the other analyzed patterns. The cellular pattern designs located on the right side of the graphs required longer fabrication time since their cells were printed one by one instead of using optimized toolpaths. Accordingly, including these pattern designs with improved trajectories into the slicing software would reduce the number of abrupt transitions of the head direction as well as filament discontinuities. This fact would also reduce the required time to manufacture most of the examined patterns and aid to the applicability of FFF cellular solids.

4.3. Finite element analysis

The Finite Element Analysis aimed to evaluate each cellular geometry's elastic performance, addressing the effect of the material model definition (orthotropic, quasi-isotropic, or isotropic) and the cell wall-thickness.

4.3.1. Cell wall-thickness

Although the deposited filament's thickness should be $t = 0.508$ mm according to the Insight 3D Printing Software preferences,

Fig. 4. Load-displacement curves for the three levels of density of the Hexachiral and Re-Entrant Hexagon I patterns. Experimental results of relative density are included.

Table 3

Compressive experimental results of elastic modulus, first peak stress, energy absorption efficiency, and Poisson's Ratio, of each cell pattern and density level tested. The results shown are average values with corresponding standard deviations. B and C are the adjusted coefficients for power-law expressions.

Pattern	Relative density (%)	Elastic Modulus (MPa)			1st Peak Stress (MPa)		Energy Abs. Efficiency (J/cm³)		Poisson's Ratio		Power-Law Adjusted Coefficients			
		E_x	E_y	E_z	σ_x^{1st}	σ_y^{1st}	W_x	W_y	ν_{xy}	ν_{yx}				
(a) Antitetrachiral[†][§]	44.58	24 ± 0	Sym.	888 ± 5	8.99 ± 2.44	Sym.	1011 ± 394	Sym.	−1.081 ± 0.001	Sym.	0.210 R^2=99.8%	Sym.	0.226 R^2=87.2%	Sym.
	25.32	4 ± 0		484 ± 5	0.42 ± 0.00		129 ± 2		−0.431 ± 0.026					
	16.60	2 ± 0		350 ± 2	0.18 ± 0.02		78 ± 19		−0.785 ± 0.009					
(b) Circular[§]	47.64	348 ± 19	274 ± 38	882 ± 63	18.02 ± 1.07	15.58 ± 0.38	1011 ± 299	782 ± 29	0.324 ± 0.007	0.298 ± 0.010	2.696 R^2=88.5%	2.099 R^2=90.1%	0.370 R^2=69.5%	0.332 R^2=75.6%
	40.18	262 ± 23	209 ± 55	842 ± 42	6.90 ± 1.85	6.86 ± 0.64	314 ± 240	356 ± 183	0.362 ± 0.009	0.198 ± 0.002				
	34.21	151 ± 3	101 ± 16	624 ± 2	7.79 ± 0.68	7.19 ± 0.61	697 ± 48	501 ± 75	0.465 ± 0.006	0.350 ± 0.011				
(c) Hexachiral[†][§]	38.61	101 ± 3	96 ± 9	716 ± 64	3.86 ± 0.31	3.42 ± 0.25	234 ± 35	204 ± 56	−0.068 ± 0.002	−0.188 ± 0.001	1.370 R^2=100.0%	1.284 R^2=99.7%	0.134 R^2=95.0%	0.123 R^2=97.3%
	27.18	36 ± 1	32 ± 0	532 ± 17	1.49 ± 0.07	1.63 ± 0.05	131 ± 5	222 ± 41	−0.130 ± 0.003	−0.219 ± 0.005				
	21.81	19 ± 2	14 ± 0	457 ± 34	0.84 ± 0.06	0.76 ± 0.13	101 ± 18	104 ± 33	−0.531 ± 0.001	−0.320 ± 0.003				
(d) Hexagon[§]	25.25	36 ± 2	Sym.	434 ± 3	1.25 ± 0.30	Sym.	138 ± 100	Sym.	0.823 ± 0.015	Sym.	1.746 R^2=99.6%	Sym.	0.110 R^2=87.6%	Sym.
	21.50	23 ± 1		390 ± 7	1.06 ± 0.10		170 ± 28		0.672 ± 0.002					
	16.44	9 ± 1		320 ± 3	0.35 ± 0.02		45 ± 8		0.757 ± 0.006					
(e) LozengeGrids[†][§]	32.60	17 ± 2	Sym.	593 ± 10	1.35 ± 0.00	Sym.	258 ± 28	Sym.	−0.007 ± 0.002	Sym.	0.396 R^2=97.1%	Sym.	0.063 R^2=90.1%	Sym.
	24.76	9 ± 1		480 ± 12	0.56 ± 0.02		168 ± 21		−0.035 ± 0.003					
	20.90	5 ± 0		394 ± 0	0.37 ± 0.00		145 ± 15		−0.021 ± 0.007					
(f) Re − EntrantHexagonI[†][§]	35.59	107 ± 7	83 ± 6	640 ± 21	3.06 ± 0.03	2.38 ± 0.18	194 ± 19	108 ± 25	−0.147 ± 0.013	−0.110 ± 0.003	1.871 R^2=99.0%	1.469 R^2=98.2%	0.125 R^2=94.3%	0.101 R^2=96.8%
	30.02	69 ± 0	56 ± 3	597 ± 23	1.92 ± 0.05	1.66 ± 0.09	144 ± 8	105 ± 2	−0.139 ± 0.004	−0.251 ± 0.010				
	20.81	17 ± 1	13 ± 1	423 ± 24	0.64 ± 0.07	0.57 ± 0.02	76 ± 21	76 ± 3	−0.132 ± 0.016	−0.306 ± 0.006				
(g) Re − EntrantHexagonII[†][§]	37.17	14 ± 1	81 ± 1	705 ± 0	0.96 ± 0.01	2.26 ± 0.00	108 ± 5	144 ± 1	−0.334 ± 0.001	−2.076 ± 0.010	0.213 R^2=99.2%	1.320 R^2=70.9%	0.040 R^2=96.1%	0.092 R^2=97.2%
	29.76	7 ± 0	48 ± 4	559 ± 7	0.70 ± 0.03	1.47 ± 0.04	142 ± 15	140 ± 8	−0.264 ± 0.006	−2.511 ± 0.008				
	25.33	5 ± 0	42 ± 1	430 ± 78	0.47 ± 0.06	1.19 ± 0.05	102 ± 29	126 ± 10	−0.147 ± 0.043	−2.483 ± 0.014				
(h) Rotachiral[†][§]	37.22	33 ± 4	Sym.	672 ± 25	2.02 ± 0.20	Sym.	250 ± 71	Sym.	−0.080 ± 0.002	Sym.	0.489 R^2=98.4%	Sym.	0.076 R^2=95.5%	Sym.
	29.26	14 ± 1		547 ± 8	1.12 ± 0.07		156 ± 22		−0.020 ± 0.007					
	23.06	9 ± 1		415 ± 24	0.55 ± 0.04		98 ± 14		−0.024 ± 0.003					
(i) SinusoidalLigaments[†][‡]	46.15	32 ± 6	Sym.	793 ± 11	10.87 ± 0.28	Sym.	3060 ± 32	Sym.	−0.029 ± 0.019	Sym.	0.060 R^2=63.9%	Sym.	0.094 R^2=59.5%	Sym.
	33.92	29 ± 9		589 ± 7	3.10 ± 0.31		446 ± 77		−0.116 ± 0.040					
	20.05	19 ± 0		416 ± 10	1.13 ± 0.04		201 ± 5		−0.118 ± 0.028					
(j) SquareGrids[†][§]	36.73	5 ± 1	Sym.	665 ± 9	2.71 ± 0.43	Sym.	642 ± 186	Sym.	−0.105 ± 0.031	Sym.	0.076 R^2=98.3%	Sym.	0.108 R^2=98.7%	Sym.
	28.72	2 ± 0		515 ± 31	1.49 ± 0.22		431 ± 75		−0.056 ± 0.019					
	20.42	1 ± 0		443 ± 4	0.87 ± 0.08		312 ± 3		−0.028 ± 0.008					
(k) SrCuBO[‡]	39.83	203 ± 13	Sym.	733 ± 37	6.72 ± 1.30	Sym.	281 ± 117	Sym.	0.223 ± 0.004	Sym.	0.363 R^2=85.4%	Sym.	0.083 R^2=74.5%	Sym.
	31.38	145 ± 20		507 ± 5	4.90 ± 0.80		369 ± 26		0.200 ± 0.002					
	23.68	83 ± 4		437 ± 6	2.06 ± 0.20		172 ± 2		0.194 ± 0.002					
(l) Tetrachiral[§]	28.23	38 ± 6	Sym.	577 ± 6	1.80 ± 0.07	Sym.	294 ± 3	Sym.	0.102 ± 0.002	Sym.	1.352 R^2=98.9%	Sym.	0.117 R^2=94.9%	Sym.
	23.34	24 ± 0		458 ± 7	1.06 ± 0.08		194 ± 10		0.056 ± 0.003					
	17.15	9 ± 0		338 ± 8	0.47 ± 0.02		147 ± 1		0.039 ± 0.001					
(m) Sparse[§]	69.13	418 ± 3	Sym.	871 ± 23	17.22 ± 0.00	Sym.	727 ± 18	Sym.	0.614 ± 0.067	Sym.	1.044 R^2=96.7%	Sym.	0.210 R^2=97.6%	Sym.
	53.02	228 ± 18		548 ± 13	11.68 ± 0.02		1425 ± 57		0.151 ± 0.042					
	42.76	155 ± 2		385 ± 3	7.89 ± 0.09		1270 ± 8		0.268 ± 0.030					
	27.71	46 ± 0		178 ± 1	2.89 ± 0.03		1663 ± 50		1.031 ± 0.113					
	16.93	10 ± 1		43 ± 0	0.79 ± 0.02		937 ± 77		0.814 ± 0.077					
	10.46	3 ± 0		34 ± 1	0.13 ± 0.01		75 ± 10		1.327 ± 0.101					
(s) Solid	100.00	1286 ± 0	Sym.	1905 ± 0	181[a]	Sym.	–	Sym.	0.554 ± 0.040	Sym.	–	–	–	–

† Auxetic cell pattern.
‡ Stretching-dominated pattern.
§ Bending-dominated pattern.
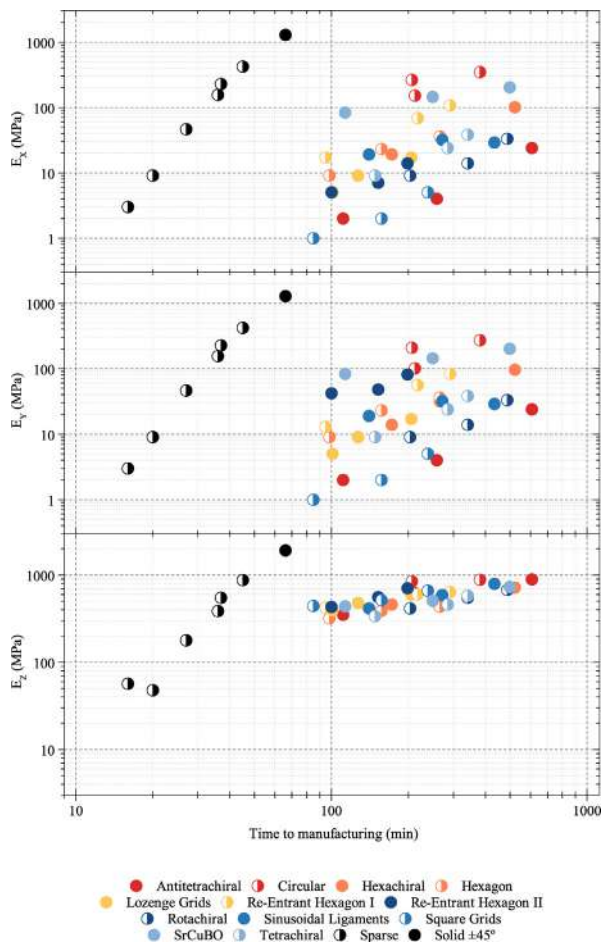[a] ASTM D695 Compressive Strength, Ultimate (Method 1, 0.05″/min) [63].

Fig. 5. Relation between the elastic modulus experimental results versus the manufacturing time for each pattern. See Fig. 1 and Tables 1 and 3 for more detail.
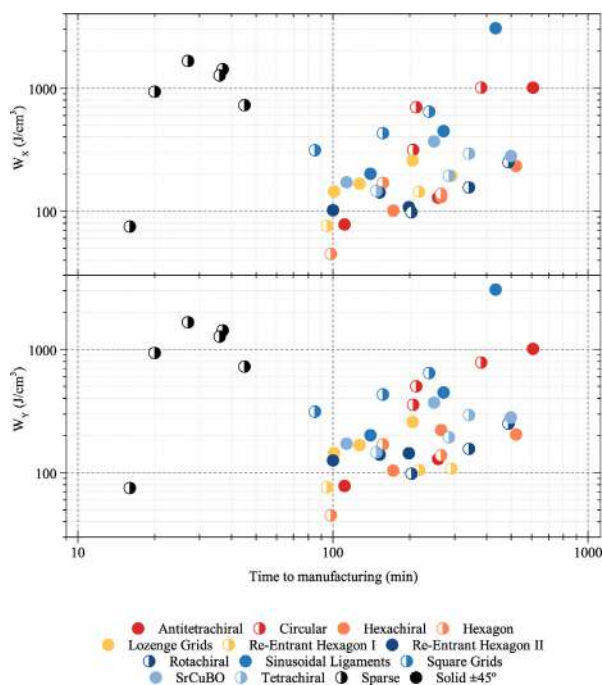

Fig. 6. Relation between the energy absorption efficiency experimental results versus the manufacturing time for each pattern. See Fig. 1 and Tables 1 and 3 for more detail.

walls in the patterns' CAD design must be widened to $t = 0.60$ mm to generate the fabrication toolpaths correctly. Nevertheless, the thickness measured on the microscopic analysis was $t = 0.5777$ mm. Hence, the three wall-thicknesses were assessed together with the three material models to conclude their effect on the mechanical behavior.

A total of 864 different models were simulated. Fig. 7 shows the boxplot diagram depicting the deviation between the numerical and experimental elastic modulus for each wall-thickness and material model considered. As can be seen, the boxplot diagram displays more widespread whiskers or a higher number of outliers when the Isotropic model is used, regardless of the wall-thickness. Besides, minor differences are observed when Quasi-Isotropic and Orthotropic models are compared. Therefore, using the Quasi-Isotropic model material allows simplifying the FFF material's model complexity without meaning noticeable variances regarding the Orthotropic model results. The results also show that wall-thickness plays a significant role in cellular solids' stiffness, as expected. Experimentally measured thickness $\{t = 0.5777\}$ mm has achieved the highest accuracy in both the Quasi-Isotropic and Orthotropic models. In particular, more than half of the Quasi-Isotropic simulations exhibited less than 10% of deviation when using the experimental t.

4.3.2. Compressive behavior

Table 4 compares the numerical, experimental, and analytical results of the cellular solids' stiffnesses in each of the three test directions, as well as the in-plane first peak stress experimental data. Numerical results were obtained considering the Quasi-Isotropic model and a wall-thickness $t = 0.5777$ mm. The analytical results in z-direction were calculated using Eq. 1 for each pattern and density level, except for the Sparse infill, as explained in Section 4.4. Power-law (Eq. 2 and Eq. 23) results are also included. The agreement of the results enables the validation of the developed FE model and the analytical equations. The differences observed between the experimental data and the estimated results from the power-law expressions are attributed to the identified manufacturing defects.

Fig. 8 (left) depicts a comparison between the simulated deformed shape and the recorded images using DIC of Antitetrachi-
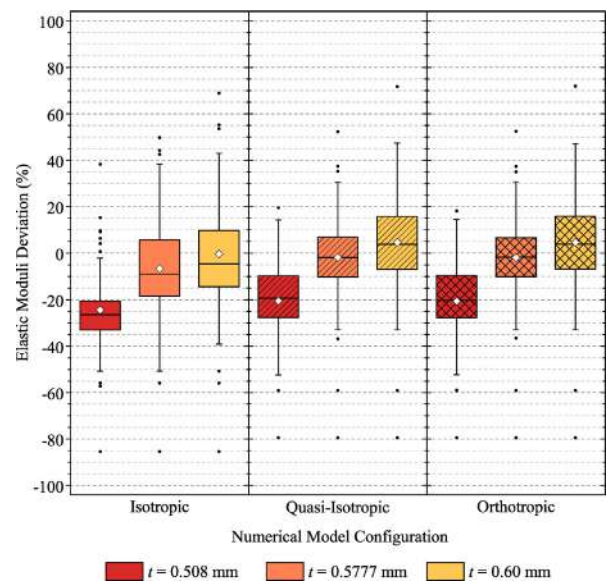

Fig. 7. Boxplot diagrams depicting the deviation of the elastic moduli between the FE model results and the experimental data for different material models and cell wall-thickness.

Table 4
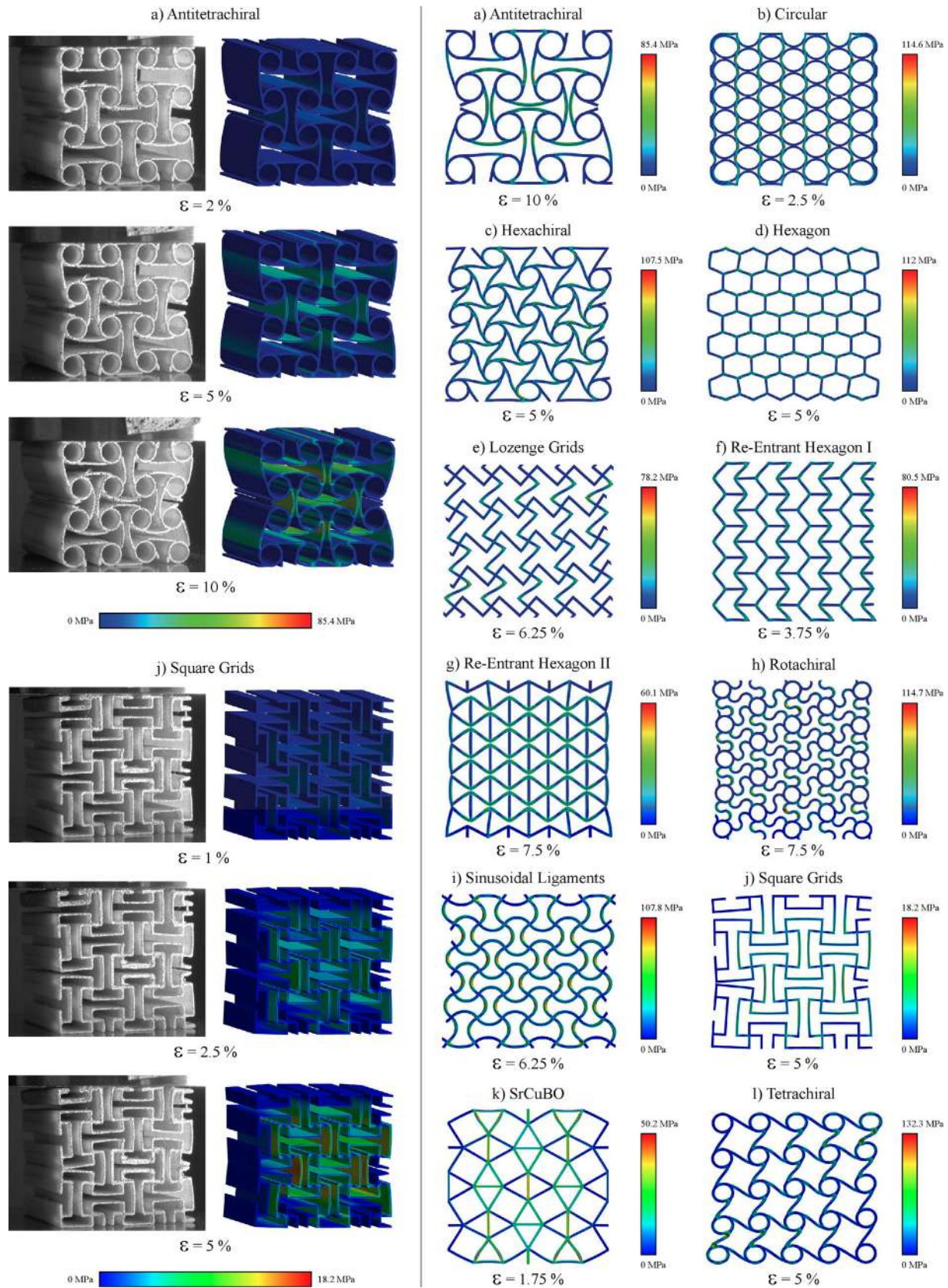Comparison of analytical, experimental and numerical results.

Pattern	Relative density (%)	E_x (MPa)			E_y (MPa)			E_z (MPa)			σ_x (MPa)		σ_y (MPa)	
		Power-Law	Num.	Exp.	Power-Law	Num.	Exp.	Analytical	Num.	Exp.	Power-Law	Exp.	Power-Law	Exp.
(a) Antitetrachiral†§	44.58	24	24	24 ± 0		Sym.		877	801	888 ± 5	8.14	8.99		Sym.
	25.32	4	6	4 ± 0				503	483	484 ± 5	2.63	0.42		
	16.60	1	3	2 ± 0				357	363	350 ± 2	1.13	0.18		
(b) Circular§	47.64	375	328	348 ± 19	292	284	274 ± 38	858	815	882 ± 63	15.20	18.02	13.64	15.58
	40.18	225	233	262 ± 23	175	204	209 ± 55	709	679	842 ± 42	10.82	6.90	9.70	6.86
	34.21	139	119	151 ± 3	108	102	101 ± 16	525	514	624 ± 2	7.84	7.79	7.03	7.19
(c) Hexachiral†§	38.61	101	132	101 ± 3	95	100	96 ± 9	779	711	716 ± 64	3.61	3.86	3.32	3.42
	27.18	35	34	36 ± 1	33	35	32 ± 0	574	526	532 ± 17	1.79	1.49	1.65	1.63
	21.81	18	21	19 ± 2	17	15	14 ± 0	449	411	457 ± 34	1.15	0.84	1.06	0.76
(d) Hexagon§	25.25	36	47	36 ± 2		Sym.		502	471	434 ± 3	1.27	1.25		Sym.
	21.50	22	30	23 ± 1				420	397	390 ± 7	0.92	1.06		
	16.44	10	13	9 ± 1				316	303	320 ± 3	0.54	0.35		
(e) LozengeGrids‡§	32.60	18	13	17 ± 2		Sym.		620	527	593 ± 10	1.22	1.35		Sym.
	24.76	8	6	9 ± 1				484	430	480 ± 12	0.70	0.56		
	20.90	5	4	5 ± 0				397	362	390 ± 0	0.50	0.37		
(f) Re − EntrantHexagonI†§	35.59	108	116	107 ± 7	85	83	83 ± 6	676	624	640 ± 21	2.86	3.06	2.31	2.38
	30.02	65	67	69 ± 0	51	56	56 ± 3	575	533	597 ± 23	2.03	1.92	1.65	1.66
	20.81	22	19	17 ± 1	17	15	13 ± 1	396	375	423 ± 24	0.98	0.64	0.79	0.57
(g) Re − EntrantHexagonII†§	37.17	14	13	14 ± 1	87	105	81 ± 1	731	658	705 ± 0	1.00	0.96	2.31	2.26
	29.76	7	7	7 ± 0	45	56	48 ± 4	588	537	559 ± 7	0.64	0.70	1.48	1.47
	25.33	4	5	5 ± 0	28	36	42 ± 1	487	453	430 ± 78	0.47	0.47	1.07	1.19
(h) Rotachiral†§	37.22	32	29	33 ± 4		Sym.		740	663	672 ± 25	1.91	2.02		Sym.
	29.26	16	15	14 ± 1				605	544	547 ± 8	1.18	1.12		
	23.06	8	8	9 ± 1				463	417	415 ± 24	0.73	0.55		
(i) SinusoidalLigaments‡	46.15	36	28	32 ± 6		Sym.		864	762	793 ± 11	7.89	10.87		Sym.
	33.92	26	25	29 ± 9				598	552	589 ± 7	5.80	3.10		
	20.05	15	19	19 ± 0				376	365	416 ± 10	3.43	1.13		
(j) SquareGrids†§	36.73	5	4	5 ± 1		Sym.		657	603	665 ± 9	2.65	2.71		Sym.
	28.72	2	2	2 ± 0				518	482	515 ± 31	1.62	1.49		
	20.42	1	1	1 ± 0				387	371	443 ± 4	0.82	0.87		
(k) SrCuBO‡	39.83	186	218	203 ± 13		Sym.		742	681	733 ± 37	5.98	6.72		Sym.
	31.38	146	138	145 ± 20				541	492	507 ± 5	4.71	4.90		
	23.68	110	92	83 ± 4				396	360	437 ± 6	3.56	2.06		
(l) Tetrachiral§	28.23	39	39	38 ± 6		Sym.		585	548	577 ± 6	1.68	1.80		Sym.
	23.34	22	25	24 ± 0				494	468	458 ± 7	1.15	1.06		
	17.15	9	11	9 ± 0				383	372	338 ± 8	0.62	0.47		
(m) Sparse§	69.13	444	503	418 ± 3		Sym.		928	763	871 ± 23	18.16	17.22		Sym.
	53.02	200	251	228 ± 18				547	434	548 ± 13	10.68	11.68		
	42.76	105	143	155 ± 2				361	282	385 ± 3	6.95	7.89		
	27.71	29	40	46 ± 0				147	113	178 ± 1	2.92	2.89		
	16.93	7	8	10 ± 1				50	37	43 ± 0	1.09	0.79		
	10.46	2	1	3 ± 0				15	11	34 ± 1	0.42	0.13		
(s) Solid ± 45°	100.00	–	1300	1286 ± 0		Sym.		–	1776	1905 ± 0	–	181[a]		Sym.

† Auxetic cell pattern.
‡ Stretching-dominated pattern.
§ Bending-dominated pattern.
[a] ASTM D695 Compressive Strength, Ultimate (Method 1, 0.05"/min) [63].

Fig. 8. Comparison of the experimental and numerical deformed shape sequences of the Antitetrachiral and Square Grids patterns (*left*). Deformed shape of each patterns before the first load peak or any internal contact was detected (*right*). Colormap stands for Von Mises stress.

ral and Square Grids as representative patterns at different strain stages. The sequences correspond to the *x*-direction tests with density level III. The colormap corresponds to the Von Mises stress results. This qualitative comparison shows a kinematic correspondence between the numerical and experimental results, with a marked auxetic behavior of both patterns. The numerical results allow identifying the most stressed zones and the contact points between the cell walls. Cross-sections of each analyzed pattern are shown on the right side of Fig. 8. Results correspond to the Von Misses stress before the first load peak, or any internal contact was detected. As can be seen, the patterns' deformed shapes are mostly bending-dominated. It can also be seen that some geometries display the maximum stress values at the joints of the unit cells. The localized stress values should indicate the failure zone of the material. However, experimental evidence has revealed that failure occurs mainly at the cell joints due to weaknesses and the reported manufacturing defects. In the experimental results of maximum stress shown in Table 3, the highest values of specific strength correspond to geometries as for example Circular, in whose microscopic analysis no discontinuity is observed in the trajectory of the filaments. This evidence highlights the importance of reducing defects of intra-layer joints to prevent premature pattern failure. So, once again, the importance of optimizing the printing toolpaths is justified, as it would reduce the amount of intra-layer manufacturing defects.

4.4. Verification of the numerical and analytical sparse infill model

The simple arrangement of the cell walls on the Sparse infill allows the derivation of an analytical expression to determine the relative elastic moduli in each of the test directions. Fig. 9 (*left*) illustrates the unit cell of the Sparse infill with boundary conditions corresponding to an in-plane compression test. Using an approach based on standard beam bending theory, Eq. 23 was derived to calculate the relative in-plane elastic moduli. E^s refers to the elastic modulus of the solid material.

$$\frac{E_x^*}{E_x^s} = \frac{E_y^*}{E_y^s} = \frac{2t^3}{a^3 + 3ta^2 + 4at^2 + 2t^3} \qquad (23)$$

The elastic modulus along *z*-direction deserved a different approach. Inter-layer voids were identified in Fig. 3 (*n-o*), which weaken the stiffness in the out-of-plane direction. Accordingly, the relative elastic modulus has been determined from the effective load-bearing areas in the *z*-direction as depicted in Fig. 9 (*right*), obtaining the following expression:

$$\frac{E_z^*}{E_z^s} = \frac{t^2}{(a+t)^2} \qquad (24)$$

The numerical and experimental results of the relative moduli for each Sparse infill as a function of the air gap and the analytical curves (Eq. 23 and 24) are plotted in Fig. 10 to assess the accuracy of the analytical expressions' prediction. The curve corresponding to the analytical adjustment of the relative density (Eq. 16) and its
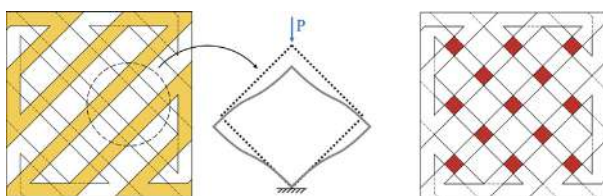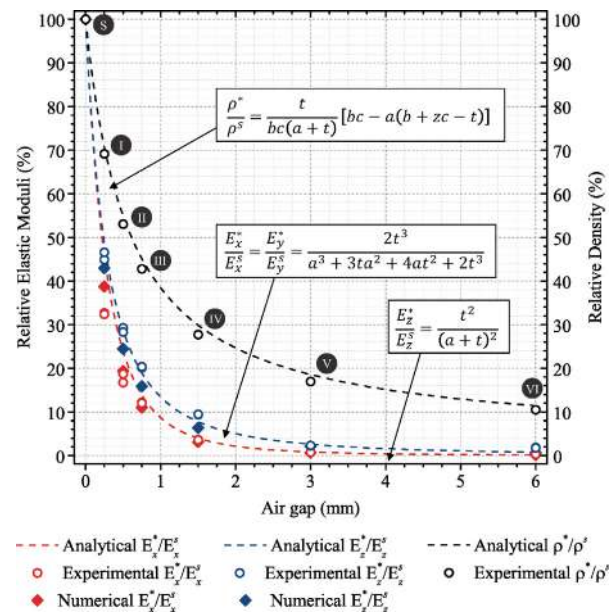

Fig. 10. Numerical, experimental, and analytical results of the relative elastic moduli and relative density of each Sparse pattern assessed in terms of the air gap.

experimental measurements are overlapped and represented on the right-hand axis.

As can be seen, the results calculated using the provided analytical equation are in good agreement with the experimental values obtained in both test directions. Furthermore, it should be noted that the analytical expression (Eq. 24) diverges from the calculation of the out-of-plane relative elastic moduli of the other cellular patterns presented in Section 2, which were obtained from a ratio of its relative density (see Eq. 1).

4.5. Comparative overall performance of FFF cellular solids

The elastic moduli results given in Table 4 are now depicted in the upper plot of Fig. 11 as a function of the relative density. The experimental densities are used for data representation. Values with diamonds correspond to numerical results, while circulars are the experimental ones. The dark shaded area states the Sparse samples' spectrum, and the red-orange area corresponds to the rest of the cellular solids. The black dots on the upper right-hand side of the graph indicate the PEI Ultem material performance, corresponding to the solid cell wall material properties.

Regarding the non-Sparse patterns, the results grouped at the top of the graph are the stiffnesses of the cellular solids in the *z*-direction, while the bottom data correspond to the *x-y* in-plane elastic moduli. The duplicity of results for the same geometry and relative density is due to the orthotropic behavior of some cell patterns. Specifically, the values at the bottom correspond to the cell's patterns with auxetic behavior. For a detailed identification of the auxetic patterns, see Table 4.

Overall, the divergence of the results for equivalent relative densities is evidence of the influence of the cellular pattern design. The results clustered at the top are related to the relative density, but the elastic *z*-modulus proves to be independent of the cell pattern. These data particularly show a good adjustment with the line plotted from the analytical Eq. 1.

Regarding the Sparse infill samples, results show a lower scatter between in-plane and out-of-plane stiffnesses. As shown, the elastic *z*-modulus of the Sparse infill is below the *z*-modulus of the other cellular geometries, as expected, and its data fit
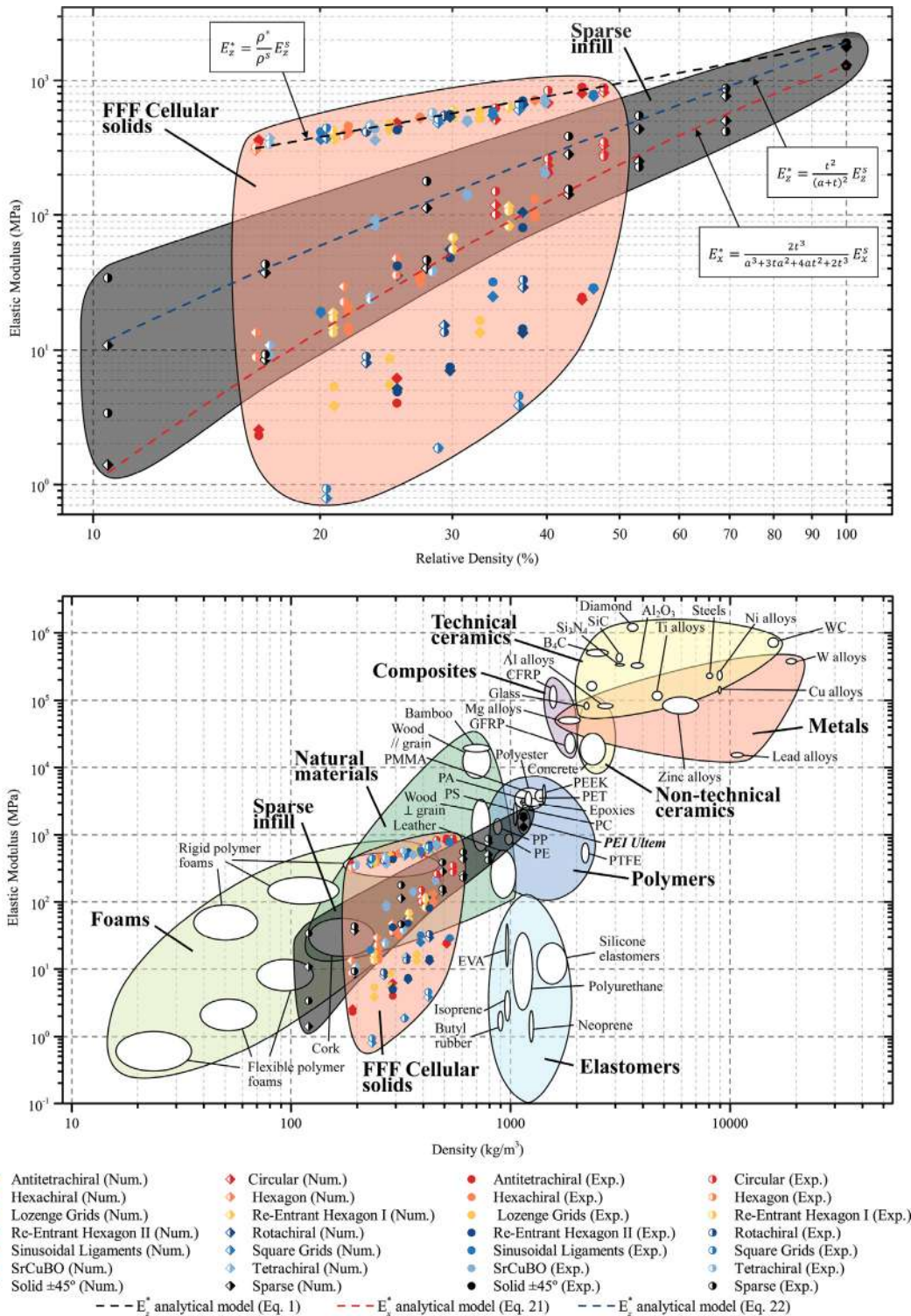

Fig. 9. Sparse pattern's cellular unit with boundary conditions corresponding to an in-plane compression test (*left*). Overlapping of two layers in the Sparse infill. The red shaded area corresponds to the contact points between layers (*right*).

Fig. 11. Material property chart including analytical, experimental and numerical results (*top*) and materials database diagram (*bottom*). Adapted from CES EduPack 2019, ANSYS Granta © 2020 Granta Design, with permission.

accurately to the curve of the proposed Eq. 24 for the relative stiffness calculation. In addition, the results achieved in experiments along *x* and *y*-directions are also in agreement with the Eq. 23 adjustment.

Lastly, to conclude the study, the stiffnesses obtained for each cellular pattern are compared to other materials as a function of

its density in the bottom graph of Fig. 11. Ansys GRANTA EduPack materials database is included for comparison. As can be seen, the specific stiffness properties of the analyzed FFF cellular solids cover a wide area that is comprised between foams, natural materials, polymers, and elastomers. The stiffnesses of the cellular solids are lower than those of the solid material, but both the geometry

and the cell size prove to play a significant role, as was intended to be demonstrated. The wide range of specific stiffnesses achieved is thus evidence of the potentials of FFF lightweight cellular solids.

5. Conclusions

This paper presents comprehensive research of the FFF technology's possibilities to create cellular solids with a broad spectrum of specific stiffness and strength, from the cell geometry and cell size, while addressing manufacturing matters such as inherent defects and manufacturing time. Thirteen typologies of two-dimensional cellular patterns with different relative densities were investigated and tested in compression in different directions, resulting in 42 different filling configurations.

The analytical approach has led to parametric equations to predict the relative density of each pattern, which have been successfully verified with experimental results. These expressions also allow the calculation of the elastic modulus in the three mutually perpendicular directions of the cells from the solid material properties.

Microscopic analysis revealed different manufacturing defects and highlighted the importance of optimizing filament trajectories. Intra-layer defects occur in certain types of cell patterns depending on their design, either due to defects in the connection of the cells or due to excessive deposition of material at filament's intersection points. Inter-layer defects are due to weak cell wall connectivity and dramatically impact the pattern's mechanical behavior when tested in the in-plane directions. To overcome these defects, it would be necessary to customize layer by layer the configuration of the filament trajectories and address its optimization.

The microscopic study also revealed the optimized arrangement of the filaments in the Sparse infill pattern, creating intentional inter-layer voids that essentially allow for a reduction in manufacturing time while maintaining satisfying mechanical properties, thus becoming an efficient solution for achieving a low-density infill.

Compression test results have allowed conclusions to be drawn regarding the influence of cell type and infill density on the mechanical performance. As expected, stiffness and stress decrease with the density of the pattern, but energy absorption efficiency does not always follow the same trend, such as in the case of the Sparse infill. Printing defects have also shown to have a critical effect on the strength of the cell patterns. Moreover, the time-to-print analysis has shown the competitive advantage of the Sparse infill over the rest of the patterns, as it provides comparable stiffness and strength properties with considerably shorter manufacturing times. This again highlights the relevance of optimizing filament trajectories in the slicing software to contribute in the application of FFF cellular solids.

The numerical study has provided a model for predicting the compressive stiffness of the different patterns, which has been validated with experimental results. The model can reproduce the behavior in the elastic range, based on tensile specimen properties and a Normal Stiffness Factor to account for the phenomenon of elastic asymmetry of the FFF printed samples. The study has evaluated the influence of the wall thickness and the material model used. The results demonstrate the validity of the hypothesis assuming a quasi-isotropic behavior of the cell wall material.

Given the outstanding behavior of the Sparse infill, its elastic performance has been deeply analyzed, obtaining analytical expressions for the calculation of the elastic moduli in the three perpendicular directions. The equations have been compared and successfully validated with numerical and experimental results. Regarding the stiffness in the out-of-plane direction, the prediction model proposed departs from approaches based on relative stiffness but shows a better correlation with experimental data.

Finally, the extensive study has allowed a reliable comparison of the elastic properties of the cellular patterns as a function of their density. The wide range of results achieved is experimental evidence of the potential of FFF lightweight cellular solids.

Data availability

The raw data required to reproduce these findings are available to download from Mendeley Data, doi: 10.17632/kf858mny8b.1. Kindly cite this article and the dataset if utilizing or modifying the data in your work.

Declaration of Competing Interest

The authors declare that they have no known competing financial interests or personal relationships that could have appeared to influence the work reported in this paper.

Acknowledgements

References

[1] L.J. Gibson, M.F. Ashby, Cellular solids - Structure and properties, second ed., Cambridge University Press, 1997.

[2] U.G. Wegst, H. Bai, E. Saiz, A.P. Tomsia, R.O. Ritchie, Bioinspired structural materials, Nat. Mater. 14 (2015) 23–36.

[3] H.N.G. Wadley, N.A. Fleck, A.G. Evans, Fabrication and structural performance of periodic cellular metal sandwich structures, Compos. Sci. Technol. 63 (2003) 2331–2343.

[4] M. Vijay Kumar, B. Soragaon, Fabrication and evaluation of multilayered polyurethane foam core sandwich panels for static flexural stiffness, Procedia Eng. 97 (2014) 1227–1236.

[5] D. Zhu, H. Shi, H. Fang, W. Liu, Y. Qi, Y. Bai, Fiber reinforced composites sandwich panels with web reinforced wood core for building floor applications, Compos. B. Eng. 150 (2018) 196–211.

[6] B. Castanie, C. Bouvet, M. Ginot, Review of composite sandwich structure in aeronautic applications, Compos. Part C. 1 (2020) 100004.

[7] J. Sargianis, H.I. Kim, J. Suhr, Natural cork agglomerate employed as an environmentally friendly solution for quiet sandwich composites, Sci. Rep. 2 (2012) 1–6.

[8] J. Banhart, H.W. Seeliger, Aluminium Foam Sandwich Panels: Metallurgy, Manufacture and Applications, Adv. Eng. Mater. 10 (2008) 3–6.

[9] R. Roy, S.J. Park, J.H. Kweon, J.H. Choi, Characterization of Nomex honeycomb core constituent material mechanical properties, Compos. Struct. 117 (2014) 255–266.

[10] X. Li, F. Lu, Y. Zhang, Y. Lin, Y. Meng, Experimental study on out-of-plane mechanical and energy absorption properties of combined hexagonal aluminum honeycombs under dynamic impact, Mater. Des. 194 (2020) 108900.

[11] Y.L. Tee, T. Maconachie, P. Pille, M. Leary, T. Do, P. Tran, From nature to additive manufacturing: Biomimicry of porcupine quill, Mater. Des. 210 (2021) 110041.

[12] Q. Liu, R. Xu, Y. Zhou, J. Ge, S. Yuan, Y. Long, T. Shi, Metamaterials mapped lightweight structures by principal stress lines and topology optimization: Methodology, additive manufacturing, ductile failure and tests, Mater. Des. 212 (2021) 110192.

[13] C.O. Ufodike, H. Wang, M.F. Ahmed, G. Dolzyk, S. Jung, Design and modeling of bamboo biomorphic structure for in-plane energy absorption improvement, Mater. Des. 205 (2021) 109736.

[14] D.J. McGregor, S. Tawfick, W.P. King, Mechanical properties of hexagonal lattice structures fabricated using continuous liquid interface production additive manufacturing, Addit. Manuf. 25 (2019) 10–18.

[15] C. Li, H. Lei, Z. Zhang, X. Zhang, H. Zhou, P. Wang, D. Fang, Architecture design of periodic truss-lattice cells for additive manufacturing, Addit. Manuf. 34 (2020) 101172.

[16] K.S. Prakash, T. Nancharaih, V.V.S. Rao, Additive Manufacturing Techniques in Manufacturing - An Overview, Mater. Today 5 (2018) 3873–3882.

[17] N. van de Werken, H. Tekinalp, P. Khanbolouki, S. Ozcan, A. Williams, M. Tehrani, Additively manufactured carbon fiber-reinforced composites: State of the art and perspective, Addit. Manuf. 31 (2020).

[18] D. Solari, I. Papallo, L. Ugga, L.M. Cavallo, I. Onofrio, R. Cuocolo, G. Improta, A. Brunetti, M. Martorelli, A. Gloria, P. Cappabianca, T. Russo, Novel concepts and strategies in skull base reconstruction after endoscopic endonasal surgery, Acta Imeko 9 (2020) 67–73.

[19] A. Forés-Garriga, M.A. Pérez, G. Gómez-Gras, G. Reyes-Pozo, Role of infill parameters on the mechanical performance and weight reduction of PEI Ultem processed by FFF, Mater. Des. 193 (2020) 108810.

[20] J.M. Chacón, M.A. Caminero, E. García-Plaza, P.J. Núez, Additive manufacturing of PLA structures using fused deposition modelling: effect of process parameters on mechanical properties and their optimal selection, Mater. Des. 124 (2017) 143–157.

[21] K. Wei, X. Xiao, J. Chen, Y. Wu, M. Li, Z. Wang, Additively manufactured bi-material metamaterial to program a wide range of thermal expansion, Mater. Des. 198 (2021) 109343.

[22] D. Downing, A. Jones, M. Brandt, M. Leary, Increased efficiency gyroid structures by tailored material distribution, Mater. Des. 197 (2021) 109096.

[23] C. Lubombo, M.A. Huneault, Effect of infill patterns on the mechanical performance of lightweight 3D-printed cellular PLA parts, Mater. Today Commun. 17 (2018) 214–228.

[24] Z.P. Sun, Y.B. Guo, V.P.W. Shim, Deformation and energy absorption characteristics of additively-manufactured polymeric lattice structures — Effects of cell topology and material anisotropy, Thin-Walled Struct. 169 (2021).

[25] S. Kumar, J. Ubaid, R. Abishera, A. Schiffer, V.S. Deshpande, Tunable Energy Absorption Characteristics of Architected Honeycombs Enabled via Additive Manufacturing, ACS Appl. Mater. Interfaces 11 (2019) 42549–42560.

[26] S.O. Obadimu, K.I. Kourousis, Compressive behaviour of additively manufactured lattice structures: A review, Aerospace 8 (2021).

[27] N. Kladovasilakis, K. Tsongas, D. Tzetzis, Mechanical and FEA-assisted characterization of fused filament fabricated triply periodic minimal surface structures, J. Compos. Sci. 5 (2021).

[28] Z. Alomar, F. Concli, Compressive behavior assessment of a newly developed circular cell-based lattice structure, Mater. Des. 205 (2021) 109716.

[29] K. Dong, H. Ke, M. Panahi-Sarmad, T. Yang, X. Huang, X. Xiao, Mechanical properties and shape memory effect of 4D printed cellular structure composite with a novel continuous fiber-reinforced printing path, Mater. Des. 198 (2021) 109303.

[30] Y. Xu, E. Schlangen, M. Luković, B. Šavija, Tunable mechanical behavior of auxetic cementitious cellular composites (CCCs): Experiments and simulations, Constr. Build. Mater. 266 (2021).

[31] Y. Jiang, B. Rudra, J. Shim, Y. Li, Limiting strain for auxeticity under large compressive Deformation: Chiral vs. re-entrant cellular solids, Int. J. Solids Struct. 162 (2019) 87–95.

[32] K.R. Olympio, F. Gandhi, Flexible skins for morphing aircraft using cellular honeycomb cores, J. Intell. Mater. Syst. Struct. 21 (2010) 1719–1735.

[33] D. Bornengo, F. Scarpa, C. Remillat, Evaluation of hexagonal chiral structure for morphing airfoil concept, Proc. Inst. Mech. Eng. G.J. Aerosp. Eng. 219 (2005) 185–192.

[34] J.J. Andrew, H. Alhashmi, A. Schiffer, S. Kumar, V.S. Deshpande, Energy absorption and self-sensing performance of 3D printed CF/PEEK cellular composites, Mater. Des. 208 (2021) 109863.

[35] S.R.G. Bates, I.R. Farrow, R.S. Trask, 3D printed polyurethane honeycombs for repeated tailored energy absorption, Mater. Des. 112 (2016) 172–183.

[36] S.R. Bates, I.R. Farrow, R.S. Trask, Compressive behaviour of 3D printed thermoplastic polyurethane honeycombs with graded densities, Mater. Des. 162 (2019) 130–142.

[37] V. Caccese, J.R. Ferguson, M.A. Edgecomb, Optimal design of honeycomb material used to mitigate head impact, Compos. Struct. 100 (2013) 404–412.

[38] Q. Ma, M.R. Rejab, A.P. Kumar, H. Fu, N.M. Kumar, J. Tang, Effect of infill pattern, density and material type of 3D printed cubic structure under quasi-static loading, Proc. Inst. Mech. Eng. C J. Mech. Eng. Sci. (2020).

[39] A. Alderson, K.L. Alderson, D. Attard, K.E. Evans, R. Gatt, J.N. Grima, W. Miller, N. Ravirala, C.W. Smith, K. Zied, Elastic constants of 3-, 4- and 6-connected chiral and anti-chiral honeycombs subject to uniaxial in-plane loading, Compos. Sci. Technol. 70 (2010) 1042–1048.

[40] F. Scarpa, S. Blain, T. Lew, D. Perrott, M. Ruzzene, J.R. Yates, Elastic buckling of hexagonal chiral cell honeycombs, Compos. Part A Appl. Sci. Manuf. 38 (2007) 280–289.

[41] L.L. Hu, M.Z. Zhou, H. Deng, Dynamic crushing response of auxetic honeycombs under large deformation: Theoretical analysis and numerical simulation, Thin-Walled Struct. 131 (2018) 373–384.

[42] S. Hou, T. Li, Z. Jia, L. Wang, Mechanical properties of sandwich composites with 3d-printed auxetic and non-auxetic lattice cores under low velocity impact, Mater. Des. 160 (2018) 1305–1321.

[43] M. Mir, M.N. Ali, J. Sami, U. Ansari, Review of mechanics and applications of auxetic structures, Adv. Mater. Sci. Eng. (2014).

[44] J.C. Álvarez Elipe, A. Díaz Lantada, Comparative study of auxetic geometries by means of computer-aided design and engineering, Smart. Mater. Struct. 21 (2012).

[45] Y. Prawoto, Seeing auxetic materials from the mechanics point of view: A structural review on the negative Poisson's ratio, Comput. Mater. Sci. 58 (2012) 140–153.

[46] Y. Liu, H. Hu, A review on auxetic structures and polymeric materials, Sci. Res. Essays 5 (2010) 1052–1063.

[47] J.N. Grima, R. Gatt, P.S. Farrugia, On the properties of auxetic meta-tetrachiral structures, Phys. Status Solidi B 245 (2008) 511–520.

[48] N. Gaspar, X.J. Ren, C.W. Smith, J.N. Grima, K.E. Evans, Novel honeycombs with auxetic behaviour, Acta Mater. 53 (2005) 2439–2445.

[49] J.P.M. Whitty, A. Alderson, P. Myler, B. Kandola, Towards the design of sandwich panel composites with enhanced mechanical and thermal properties by variation of the in-plane Poisson's ratios, Compos. Part A Appl. Sci. Manuf. 34 (2003) 525–534.

[50] F. Scarpa, P.J. Tomlin, On the transverse shear modulus of negative Poisson's ratio honeycomb structures, Fatigue Fract. Eng. Mater. Struct. 23 (2000) 717–720.

[51] N. Kladovasilakis, P. Charalampous, K. Tsongas, I. Kostavelis, D. Tzetzis, D. Tzovaras, Experimental and computational investigation of lattice sandwich structures constructed by additive manufacturing technologies, J. Manuf. Mater. Process. 5 (2021).

[52] A. Ajdari, B.H. Jahromi, J. Papadopoulos, H. Nayeb-Hashemi, A. Vaziri, Hierarchical honeycombs with tailorable properties, Int. J. Solids Struct. 49 (2012) 1413–1419.

[53] D. Mousanezhad, H. Ebrahimi, B. Haghpanah, R. Ghosh, A. Ajdari, A.M.S. Hamouda, A. Vaziri, Spiderweb honeycombs, Int. J. Solids Struct. 66 (2015) 218–227.

[54] D.M. Correa, T. Klatt, S. Cortes, M. Haberman, D. Kovar, C. Seepersad, Negative stiffness honeycombs for recoverable shock isolation, Rapid Prototyp. J. 21 (2015) 193–200.

[55] C. Lira, F. Scarpa, Y.H. Tai, J.R. Yates, Transverse shear modulus of SILICOMB cellular structures, Compos. Sci. Technol. 71 (2011) 1236–1241.

[56] N.A. Fleck, V.S. Deshpande, M.F. Ashby, Micro-architectured materials: Past, present and future, Proc. R. Soc. A 466 (2010) 2495–2516.

[57] A.J. Wang, D.L. McDowell, In-plane stiffness and yield strength of periodic metal honeycombs, J. Eng. Mater. Technol. 126 (2004) 137–156.

[58] Materialise, Ultem 9085 Datasheet, Technical Report, 2021.

[59] ASTM C365, Standard Test Method for Flatwise Compressive Properties of Sandwich Cores, ASTM International, West Conshohocken, PA (2003).

[60] P.-T.I. Inc, Ultem 1010 (Polyetherimide), Technical Report, 2011.

[61] M.M. Pastor-Artigues, F. Roure-Fernández, X. Ayneto-Gubert, J. Bonada-Bo, E. Pérez-Guindal, I. Buj-Corral, Elastic asymmetry of PLA material in FDM-printed parts: Considerations concerning experimental characterisation for use in numerical simulations, Materials 13 (2020) 1–24.

[62] C. Perkowski, Tensile-compressive asymmetry and anisotropy of fused deposition modeling PLA under monotonic conditions, Ph.D. thesis, 2017.

[63] Stratasys Inc, Ultem 9085 Production-Grade Thermoplastic for Fortus 3D Printers, Technical Report, 2017.